Evaluation of post-retrieval de-noising of active and passive microwave satellite soil moisture

Chun-Hsu Su[a,*], Sugata Y. Narsey[b], Alexander Gruber[c], Angelika Xaver[c], Daniel Chung[c], Dongryeol Ryu[a], Wolfgang Wagner[c]

[a]*Department of Infrastructure Engineering, The University of Melbourne, Parkville, Victoria, Australia*
[b]*ARC Centre of Excellence for Climate System Science, Monash University, Victoria, Australia*
[c]*Department of Geodesy and Geoinformation, Vienna University of Technology, Vienna, Austria*

Abstract

Active and passive microwave satellite remote sensing are enabling sub-daily global observations of surface soil moisture (SM) for hydrological, meteorological and climatological studies. Because the retrieved SM data can be quite noisy, post-retrieval processing such as de-noising can play an important role to aid interpretation of the observed dynamics and/or enhance their utility for data assimilation. To date, the merits of such techniques have not yet been fully evaluated. Here we consider the applications of Fourier-based de-noising filters of Su et al. (2013a) for improving SM retrieved by AMSR-E (Advanced Microwave Scanning Radiometer for Earth Observing System) and ASCAT (Advanced Scatterometer of MetOp-A) sensors. The filters are calibrated in the frequency domain based on a water-balance model, without the need for ancillary data. The evaluation of the de-noising methods was conducted globally against in situ data distributed via the International Soil Moisture Network (ISMN) at 277 AMSR-E and 385 ASCAT pixels. Systematic improvements were found for all considered metrics, namely root-mean-square deviation, linear correlation and signal-to-noise ratio, for both SM products, with improvements more striking for AMSR-E. However, the originally proposed implementation of the

---
*Corresponding author
Email address: `csu@unimelb.edu.au` (Chun-Hsu Su)

filters can induce undesirable over-smoothing and distortion of SM timeseries. To overcome this, based on a simple heuristic argument, we propose the use of ancillary precipitation data in the filtering process, although at some expense of overall agreements with the in situ data.

1. Introduction

Several space-borne active and passive microwave sensors provide frequent surface soil moisture (SM) observations under diverse land-surface and meteorological conditions. These sensors and missions include AMSR-E (Advanced Microwave Scanning Radiometer for Earth Observing System) of Aqua satellite (Njoku et al., 2003), AMSR2 (Advanced Microwave Scanning Radiometer-2) of GCOM-W1 (Global Change Observation Mission-Water) mission (Imaoka et al., 2010), SMOS (Soil Moisture and Ocean Salinity) mission (Kerr et al., 2001), SMAP (Soil Moisture Active Passive) mission (Entekhabi et al., 2010), and AS-CAT (Advanced Scatterometer) of MetOp satellites (Wagner et al., 2013). Numerous evaluation studies have demonstrated skills of these sensors to capture the SM variability observed in in situ data (e.g. Jackson et al., 2010; Albergel et al., 2012; Su et al., 2013b; Wagner et al., 2014). Given the vital role of SM in hydrological and meteorological processes in regulating water and energy exchanges and storages, satellite-retrieved SM data are increasingly being tested in rainfall-runoff modelling (e.g. Crow & Ryu, 2009; Brocca et al., 2012), numerical weather modelling (e.g. Drusch et al., 2005; Scipal et al., 2008a), and land models (e.g. Kumar et al., 2012; Draper et al., 2012).

In these applications, on one hand, accurate error characterisation of the satellite SM is required for bias correction of the observational data (Su et al., 2014a), data merging (Yilmaz et al., 2012), and optimal correction of state prediction in data assimilation (Yilmaz & Crow, 2013). On the other hand, any systematic errors of the satellite SM need to be removed during the retrieval

and the post-retrieval processes, while a low signal-to-noise ratio (SNR) can also
undermine direct interpretation of the SM dynamics and their utility for data
assimilation. In particular, field validation and error estimation using triple col-
location (TC) analysis (Scipal et al., 2008b; Dorigo et al., 2010; Draper et al.,
2013; Su et al., 2014b) have found considerable error in the satellite data, at
levels that are commensurate with or greater than that of model-simulated SM
at many regions globally. More recently, spectral analyses also indicate possible
presence of systematic periodic errors in satellite SM (Su et al., 2013a, 2014b).
While advances in sensor technology and retrieval algorithms will continue to
improve retrieval performance in the future, it is also conceivable to post-process
available SM products to reduce noise and systematic errors using appropriate
de-noising schemes.

Most SM retrieval algorithms are based on instantaneous observations. This
is because of high temporal variability of the water content in the thin remotely
sensed soil layer, and for passive microwave, the relative ease of applying radia-
tive transfer model to instantaneous measurements. However, this implies that
these algorithms do not exploit the temporal auto-correlation nature of SM using
past and/or future observations. There are now increasing attempts to rectify
this from the viewpoint of signal processing of the retrieved (level 2 or 3) geo-
physical products. In particular, Du (2012) proposed combining high-frequency
spectral components from direct sensor observations (of land emissivity) with
low-frequency outputs of land surface models or current remote sensing SM
products using Fourier filters. While shown to improve passive microwave SM
at two watersheds in the United States, the technique assumes that accurate
low-frequency components are already available. By contrast, Su et al. (2013a)
focused on reducing high-frequency random and systematic errors; they used a
linearized water balance model to develop Fourier filters to de-noise two pas-
sive and active SM products over southeast Australia. However these filters
are linear, time-invariant (LTI) filters that can lead to over-smoothing of SM
timeseries and in causal form, lead to distortion. This is problematic because
sharp increases of SM due to precipitation are important for many hydrological

3

(e.g., flood) modelling and should be preserved. More recently, Massari et al. (2014) proposed a conservative approach of using entropy-based wavelet de-noising (Sang et al., 2009) to reduce noise, based on reproducing white noise characteristics in the residuals. Evaluations over selected in situ network also show promising results. Lastly, Su & Ryu (2015) demonstrated the use of TC to provide scale-by-scale error estimates for non-linear de-noising of SM via wavelet thresholding.

The subject of this paper is the de-noising filters of Su et al. (2013a) and its objective is two-fold. Foremost, this work expands on the previous work, by presenting a comprehensive validation of two gap-filled, de-noised passive and active SM products from the AMSR-E and ASCAT instruments, against in situ data from the International Soil Moisture Network (ISMN). During the process, the utility of the data interpolation method of Garcia (2010) for in-filling gaps, as a post-retrieval step before de-noising, in the satellite data is also evaluated. Second, we propose an alternative implementation of the filters that considers a simple use of precipitation data to reduce the effect of over-smoothing and distortion introduced by the de-noising filters. This is achieved by dynamically influencing the input-output relations of the filters. The subject of this paper is the de-noising filters of Su et al. (2013a) and its objective is two-fold. Foremost, this work expands on the previous work, by presenting a comprehensive validation of two gap-filled, de-noised passive and active SM products from the AMSR-E and ASCAT instruments, against in situ data from the International Soil Moisture Network (ISMN). During the process, the utility of the data interpolation method of Garcia (2010) for in-filling gaps, as a post-retrieval step before de-noising, in the satellite data is also evaluated. Second, we propose an alternative implementation of the filters that considers a simple use of precipitation data to reduce the effect of over-smoothing and distortion introduced by the de-noising filters. This is achieved by dynamically influencing the input-output relations of the filters.

The reminder of this paper is organised as follows. Section 2 presents the satellite SM and several ancillary data sets used in this work and their pre-

processing. Section 3 reviews the de-noising schemes proposed in Su et al. (2013a) and describes the use of precipitation data in their implementation. The method for evaluating the SM data is also presented. Section 4 reports separate evaluations of gap-filled and de-noised SM data, which are further discussed in section 5. Section 5 also offers our concluding remarks.

2. Data and pre-processing

We consider the SM data from AMSR-E and ASCAT for their distinctive characteristics in terms of sensor characteristics and retrieval algorithms. The quality of these products after de-noising is assessed against in situ data from ISMN. We also explore the use of satellite-retrieved precipitation data in the de-noising process to enhance the performance of de-noising. An additional SM data from ERA-Interim model re-analysis is also needed for TC analysis with the satellite data. These 5 data sets are described in the following sections 2.1–2.5 and their pre-processing in section 2.6.

2.1. AMSR-E soil moisture

The AMSR-E sensor on the Aqua satellite enabled retrievals of surface SM at 1–2 cm depths based on observed C/X-band microwave emissions from the shallow soil surface. Most passive retrieval approaches implement an inversion of the forward radiative transfer model of a canopy-masked soil surface to convert measured brightness temperature to SM (Mladenova et al., 2014). The VUA-NASA (Vrije University Amsterdam/National Aeronautics and Space Administration) data set is used in this work. The product is based on the Land Parameter Retrieval Model (LPRM) (Owe et al., 2008), which uses the radiometer's dual-polarization observations to estimate the vegetation optical thickness and the soil dielectric constant simultaneously. A dielectric mixing model is then applied to relate the dielectric constant to volumetric SM in units of m^3m^{-3}. The latest version (v) 5, Level 3 gridded, twice-daily, C-band SM data set is expressed on a regular $1/4° \times 1/4°$ spatial grid for the period of

5

June 2002–October 2011. The data was screened based on the accompanying

₁₁₅ quality flag to identify swath edge effects, frozen or thawing soil, radio frequency interference, and dense vegetation. Screening for non-zero snow depth based on ERA-Interim SM (see section 2.4) was also conducted. The pixels > 10% urban and water cover and > 10% topographic complexity were omitted from this study. The urban and water cover information comes from Glob-

₁₂₀ Cover (Arino et al., 2007) (v2.3), Global Lakes and Wetlands Database (GLWD) (Lehner & Döll, 2004), and Global Self-consistent, Hierarchical, High-resolution Shoreline (GSHHS v1.5) database.

2.2. ASCAT soil moisture

The ASCAT sensor of the MetOp-A satellite uses the backscatter at C-

₁₂₅ band to estimate SM, as the backscatter is sensitive to the moisture content of the scattering land surface. By using a timeseries-based change-detection algorithm (Wagner et al., 1999), the SM can be measured relative to historical minima and maxima, as a percentage of saturation within these bounds. This approach is less susceptible to the influence of surface roughness as its

₁₃₀ variability occurs over a time scale longer than SM, and the influence of vegetation is taken into account by the algorithm. We use the ASCAT data set (January 2007–December 2013) produced using the Soil Water Retrieval Package (WARP) (Naeimi et al., 2009) (v5.5) from Vienna University of Technology (TU-Wien). The product is defined over a sinusoidal grid with a grid reso-

₁₃₅ lution of ∼ 12.5 km. Before use, the data was screened using its dynamical quality flag for frozen surface and temporary standing water. And as with the AMSR-E data, further screening based on snow depth, urban and water cover and topographic complexity was also applied.

2.3. In situ soil moisture

₁₄₀ The International Soil Moisture Network (ISMN) collects in situ SM measurements from 42 operational and experimental monitoring networks worldwide and acts as a single channel in data delivery (Dorigo et al., 2011). The extensive

6

list of data providers and networks is reported in Gruber et al. (2013) and references therein. While most of the networks are located in Northern America and Eurasian, some regions in Australia and Africa are also monitored. Importantly, the spatial coverage of these networks provides a variety of climatic regions, land cover types and soil textures for global scale validation. However, as the monitoring implementations differ across (and also within) the networks in terms of the sensors, installation depths and quality controls, the ISMN performed pre-processing to ensure data consistency in terms of units, sampling interval, data format, quality control, and metadata. First, the in situ data were harmonized in units of volumetric SM (m^3m^{-3}) and temporal resolution. Then, quality check was carried out to ensure SM values are within geophysical dynamic ranges and are consistent with changes in soil temperature and precipitation. SM estimates were also analysed and flagged for spikes, positive and negative breaks, signal saturation and unresponsive sensors. These resulted in quality flags added to the data. For more details, consult Dorigo et al. (2013). We use the database downloaded in May 2014 and the harmonized uppermost layer SM data at depths ranging from 0–40 cm. For our evaluation purpose, the ISMN data were screened using the added quality flags such that we retained the data that was not flagged by the quality control process; these are the data identified with a 'U' flag as per `http://ismn.geo.tuwien.ac.at/data-access/quality-flags`.

2.4. ERA-Interim soil moisture

ERA-Interim is an atmospheric, ocean and land surface reanalysis produced by ECMWF (European Centre for Median-range Weather Forecasts) based on their Integrated Forecast System (IFS) model (Dee et al., 2011). It covers the time period of 1979–present and has a T255 horizontal resolution ($\sim 0.7°$ at the equator). SM estimates are provided for 4 different layers, 4 times per day at 0, 6, 12, and 18h UTC. The data for the HTESSEL land surface scheme was used for its more realistic representation of different soil types. The uppermost layer SM estimates in units of volumetric SM (m^3m^{-3}) at depths 0–7 cm are used and the ERA pixels are spatially co-located with AMSR-E and ASCAT pixels via

nearest-neighbour rule, and the ERA SM timeseries were linearly interpolated to match the times of the satellite observations. We note ERA SM is only used for data screening (see sections 2.1, 2.2 and 2.6) and TC analyses (section 3.3) during evaluation.

2.5. Precipitation

The TRMM (Tropical Rainfall Measuring Mission) Multisatellite Precipitation Analysis (TMPA) combined precipitation estimates from multiple satellites and monthly gauge analyses at $1/4° \times 1/4°$ spatial grid resolution and 3-hourly temporal resolution (Huffman et al., 2007). The method combines estimates from four passive microwave sensors (including AMSR-E) of low-earth orbit satellites and infrared data from geosynchronous-earth orbit satellites. Altogether, they provide on average 80% of the earth's surface over the latitude of $50°$ to $-50°$. Contrary to the real-time 3B42 Real-Time (RT) data set, the TMPA retrospective data set 3B42 uses the Global Precipitation Climatology Center (GPCC) monthly monitoring product to provide gauge adjustment. We use the latest v7 TMPA 3B42 data set that has a temporal coverage from 1998.

2.6. Data pre-processing

The pre-processing of AMSR-E and ASCAT data are needed and were performed separately, as were their de-noising and evaluation. The grid resolutions of satellite SM and rainfall, ERA, and in situ SM data are variable. The co-location of the satellite data and model data was determined by nearest-neighbour association. The matchup of the satellite SM data with a single co-located monitoring station is however based on linear correlation significance analysis using ground (θ_I), ERA (θ_M), and satellite SM data (θ_S), with a probability threshold of 0.05. First, in the screening step, ground sensors were discarded as being non-representative at the coarse scale when the Pearson's correlation $R(\theta_S, \theta_M)$ is significant, while $R(\theta_I, \theta_S)$ and $R(\theta_I, \theta_M)$ are not. Then if there are multiple valid stations co-located in a satellite pixel, the station with the highest mean correlation to the satellite and ERA SM was retained. Note

that linear correlation is used to measure representativeness because the metrics used in our evaluation (section 3.3) are similarly based on a linear model.

Given that AMSR-E had a revisit time of 1–2 days and ASCAT has 1–3 days, the overpass times of the respective satellites are irregular and the timing of each half-orbit pass can have 1–2 hour offsets. For conventional spectral analysis and de-noising (see section 3.1), a regularly spaced timeseries is necessary. At each satellite pixel, frequency analyses of the corresponding overpass times were conducted to identify the most frequent ascending and descending overpass times of the satellites. These times were then used to define a 12-hourly regular temporal grid (in UTC) upon which the satellite data was regridded.

In-filling of the missing values is also needed. A one-dimensional interpolation algorithm based on discrete cosine transform (DCT) (Wang et al., 2012) was applied to infill gaps of lengths ≤ 5 days. Contrary to the traditional methods based on nearest-neighbour, polynomial or spline local interpolations, the missing data were assigned values that are estimated using the entire timeseries (Garcia, 2010). The signal and noise information may be largely preserved, but the possibilities of smoothing (see section 4.1) and generating autocorrelated errors still exist. Thus, pixels with excessive gaps should be omitted, such that we require that at least 80% of continuous gaps at a pixel are ≤ 2-day long. It is beyond the scope of this work to examine the dependency of the performance of the interpolation scheme on the length of the gaps and the auto-correlation length of local SM signal. Lastly, the satellite data was further sifted for locations with sufficiently long, continuous timeseries for calibration of the de-noising filters (see section 3.1), and a threshold of 180-day was adopted. Consequently, de-noising was applied to 289 AMSR-E pixels and 387 ASCAT pixels, but the actual number of pixels that can be evaluated depends on the availability of in situ data (section 3.3).

3. Methods

Section 3.1 provides a brief review of the concept of LTI filters, and the principles and the standard implementations of de-noising filters (Eqs. 4, 5, 7) proposed by Su et al. (2013a). Section 3.2 presents a new methodological development (Eq. 8), based on using the precipitation data in the filter implementations to overcome the shortcomings of the standard implementations. Section 3.3 describes our evaluation methodology.

3.1. De-noising filters

Consider the noisy data $\theta_i[n]$ with its z-transform $\Theta_i(z)$, where the data is regularly spaced at time intervals $t \equiv n\Delta t$ ($n \in Z$) and the frequency variable $z \equiv \exp(i\omega) \in \mathcal{C}$ is expressed in terms of angular frequency $\omega \equiv 2\pi/T$ or period T. As an input to a linear and time-invariant (LTI) filter, the filter generates an output $\theta_o[n]$ and a transform $\Theta_o(z)$ via a convolution summation between the input and an impulse function $h[n]$,

$$\theta_o[n] = (h * \theta_i)[n] \equiv \sum_{m=-\infty}^{\infty} h[m]\theta_i[n-m]. \tag{1}$$

where $h[n]$ describes the relative weights to be applied to the past and future values of the input timeseries in informing the present values of the output timeseries. An equivalent picture of the filter operation is in the frequency domain, where the input-output relation in Eq. 1 can be expressed as,

$$\Theta_o(z) = H(z)\Theta_i(z) \tag{2}$$

with $H(z)$ being the z-transform of the impulse response $h[n]$. It therefore describes how to change the frequency content of θ_i. The rescaling of the values of individual Fourier coefficients of the input data allows either suppression of selected frequency components if $|H(z)| < 1$ or shift in time by $\angle H(z)/\omega$, where $|H|$ is the modulus of H and $\angle H$ is its angle. The task is therefore to specify a suitable H to remove the stochastic error in satellite data. Two types of de-noising filters were proposed as follows.

3.1.1. Wiener filters

255   The first type of filters is the Wiener filters (Wiener , 1964). For de-noising SM data, they were developed based on the rationale that the signal in an erroneous SM timeseries should have the spectral properties of a water balance model. Importantly, the SM dynamics at any spatial scale (point-to-satellite footprint) is governed by the water balance equation (Salvucci, 2001), $d\theta/dt =$

260   $p - l$, where θ is the SM in units of volumetric SM $[L^3L^{-3}]$, p is the throughfall precipitation and l is the loss term. The power spectral density (PSD) of the equation under linear approximations has a brown spectrum of $S_\theta(\omega) = S_p/(\eta^2 + \omega^2)$ (Katul, 2007), where $S_\theta(\omega)$ has units of $[L^6L^{-6}T/rad]$. Here, S_p is directly related to the transform of precipitation and has units of $[L^6L^{-6}rad/T]$, and

265   η is the effective SM loss rate and has been recast as a quantity with units of $[rad/T]$. Despite the explicit use of volumetric SM units here, θ and S_θ can be rescaled arbitrarily into other units, such as percentage of saturation for use with ASCAT. As illustrated in Fig. 1, this theoretical PSD contrasts with the empirical PSD of AMSR-E and ASCAT SM, which show a spectrally distinctive

270   'noise floor' in the high-frequency regime. The corresponding timeseries plots are shown in Fig. 2, with the satellite SM showing greater variability relative to in situ SM over short-time periods. The contribution of the high-frequency noise to the observed PSD can be modelled as white noise, leading to a spectral model of an erroneous SM data,

$$S'_\theta(\omega > 0) = \frac{S_p + 2\eta\sqrt{S_p S_E}}{\eta^2 + \omega^2} + S_E \tag{3}$$

275   where S_E is the PSD of the error and has units of $[L^6L^{-6}T/rad]$. Recently, Su et al. (2014b) have demonstrated that the application of this signal-noise model to estimate satellite error is complementary to the TC analysis. But, it is also apparent from the satellite PSDs that the satellite error has high-frequency spectral structures more complicated than that of a white-noise model.

280   Based on the model in Eq. 3, the Wiener filter formalism provides the linear minimum mean-square error (LMMSE) solution of recovering the expected brown spectrum at filter output θ_o (Su et al., 2013a). Accordingly, its solution

11

is a symmetric exponential filter equation, namely

$$\theta_o[n] \quad = \quad \frac{1 - e^{-\gamma}}{2} \Big\{ \sum_{m=0}^{\infty} e^{-\gamma m} \theta_i[n - m] + \tag{4}$$

$$\sum_{m=0}^{\infty} e^{-\gamma m} \theta_i[n + m] \Big\}$$

where $\gamma \equiv \sqrt{S_p/S_E + \eta^2}$ is the single filter coefficient [rad/T]. We note that the multiplicative constant of Eq. 4 differs from that reported in Su et al. (2013a) because an additional renormalisation condition $H(\omega = 0) = 1$ is imposed here to ensure that the mean of θ_i is preserved in θ_o. Since the geometric series has the identity $\sum_{m=0}^{\infty} e^{-\gamma m} = 1 - e^{\gamma}$, the renormalisation implies that the sum of weights equates unity. By the same argument, where the summations in Eq. 4 are necessarily truncated for finite data, we impose that the same normalisation condition to ensure the mean is preserved. It is also true when there are missing values in the input timeseries.

The Wiener filter coefficient γ is determined by fitting the spectral model parameters $\{S_p, S_E, \eta\}$ of Eq. 3 to the empirical PSD of the input SM data using nonlinear least-squares minimization; thus, no ancillary data is required. For more details on model fitting, consult Su et al. (2014b). The empirical PSD is calculated using the Welch's method with a Hamming window of size $W = \min(L, 365)$ in units of days. $L \geq 180$ is the length of the timeseries, and we require a minimum of 180-day timeseries for de-noising. The fitted models to the AMSR-E and ASCAT PSDs are illustrated by the solid blue curves in Fig. 1, comparing with the dashed blue curves if noise is absent from the satellite data. It is also of note that other error estimators such as TC can also be used to provide knowledge of the noise parameter S_E (Su et al., 2014a).

The Wiener filter of Eq. 4 is a low-pass filter that suppresses the high-frequency components and does not cause distortion, since its transfer function has the properties $H(\omega \ll \eta) \to 1$, $H(\omega \gg \eta) \to 0$, and the angle $\angle H(\omega) = 0$. The filter is also non-causal (NC) or a "smoother" as it operates upon the future of the input timeseries (the second term of Eq. 4), and thus can only be used in data re-analysis. Consequently, a causal (C) form of the Wiener filter was

12

developed, namely

$$\theta_o[n] = (1 - e^{-\gamma}) \sum_{m=0}^{\infty} e^{-\gamma m} \theta_i[n - m] \tag{5}$$

which has also been renormalised. In a recursive form, the filter equation becomes,

$$\theta_o[n] = e^{-\gamma}\theta_o[n] + (1 - e^{-\gamma})\theta_i[n]. \tag{6}$$

The causal Wiener filter is also a low-pass filter with same gain properties as the non-causal counterpart. Furthermore, it is mathematically equivalent to the SWI (soil water index) filter used in estimating profile SM from surface SM (Wagner et al., 1999; Albergel et al., 2008). But, the Wiener filters are solutions to the signal estimation problem from the viewpoint of digital signal processing, producing SM estimates at the representative sampling depth of the sensors, e.g., 1–2 cm for C-band of AMSR-E and ASCAT. By contrast, the SWI filter conceptually yields SM estimates at a different depth characterized by a time constant, and is typically calibrated against in situ observations (Albergel et al., 2008).

The causal filter can lead to distortion at the output because of the time delay caused by the filter ($\angle H(\omega) \neq 0$). Other caveats should also be noted for both causal and non-causal filters. The optimality of the LTI Wiener filtering requires stationarity of the signal and noise components that made up θ_i, while SM is generally non-stationary and retrieval errors can vary with land surface conditions (e.g. Su et al., 2014b). Being the LMMSE solutions developed under linear approximation to the water balance equation, they fail to account for non-linear dynamics due to surface saturation and dynamical hydraulic conductivity. Consequently, their applications can lead to auto-correlated errors in θ_o and over-smoothed SM with suppressed rainfall wet-up dynamics.

3.1.2. Bandstop filters

The second type of filters is the bandstop filters that reject specific frequency components at ω_j in satellite SM. Its transfer function therefore has the properties $H(\omega_j) \approx 0$ and $H(\omega \neq \omega_j) \approx 1$. As shown in Fig. 1a-c, it is needed to

13

remove the extraneous peaks in the AMSR-E's PSDs with periods T ranging from 1–8 days. These systematic errors should not be confused with systematic additive or multiplicative biases. Rather, they correspond to possible persistent oscillations in the time domain. The input-output equation of the simplest bandstop filter is,

$$
\begin{aligned}
\theta_o[n] \quad = \quad & 2r_j \cos \omega_j \theta_o[n-1] - r_j^2 \theta_o[n-2] + \\
& H_0(\theta_i[n] - 2 \cos \omega_j \theta_i[n-1] + \theta_i[n-2])
\end{aligned}
\tag{7}
$$

where the coefficient r_j adjusts the bandwidth of the filter and H_0 provides renormalization. For simplicity, a constant $r_j = 0.98$ is used, corresponding to a full width of 0.022 rad/h at half maximum that is narrow relative to the spectral range of 0.26 rad/h for a half-daily timeseries. In this work we apply the bandstop filter only to the AMSR-E data, as pronounced spectral peaks can not be easily identified in the ASCAT data, e.g., see Fig. 1d-f. A short Hamming window of 90-day is used to estimate its PSD at high-frequency regime, over which the frequencies of the systematic periodic errors are identified using a peak-finding algorithm.

3.2. Filtering with precipitation data

Given that the Wiener filtering can produce over-smoothed and/or distorted SM timeseries, we consider the use of the ancillary precipitation data to modify its implementation. The rationale is as follows. SM can show strong auto-correlation due to the relatively slow transient behaviour of drainage and evapotranspiration, whereas rainfall wetting decreases this auto-correlation. In particular, when sampled frequently between any two consecutive rainfall events, the SM values are strongly correlated in time. But, the SM values before and after a rainfall event typically have little correlation due stochastic nature of rainfall amount and duration, and the nonlinear saturation threshold.

Suppose then a SM timeseries being segmented into different time periods, each with absence of rainfall occurrence. The start of each period Φ is signaled by a rainfall event, and its end precedes the next event. Recall that the filtering

14

equations (Eqs. 1, 4, 5, 7) relate an output (filtered) SM value $\theta_o[n]$ at time step n of the period Φ to current input SM value $\theta_i[n]$ at time n, as well as the surrounding SM values in time $\theta_i[n \pm m]$ for some m. Yet, the above heuristic argument suggests that the input SM values residing outside the period Φ should have weak influence on SM within it. Hence it is reasonable to adopt a conditional input-output relation where the filter output at time step $n \in \Phi$ is given by,

$$\theta_o[n] = \sum_{(n-m) \in \Phi} h[m]\theta_i[n - m], \qquad (8)$$

c.f. Eq. 1. This means that the backward summation (with positive m) is truncated at the start of the period Φ and for the non-causal filter, the forward summation (with negative m) is truncated at the end of the period. With the truncation, renormalisation was applied at each n so that the sum of the weighting $h[m]$ is unity. By using Eq. 8, greater amount of SM information in Φ is preserved at the output $\theta_o[n]$ for $n \in \Phi$. For the causal (Wiener and bandstop) filters, it can be observed that $\theta_o[n] = \theta_i[n]$ if there is a rainfall occurrence at n, i.e. the output retains all the information in the input. Such an implementation of the causal Wiener filtering further highlights its functional difference from the SWI filter. Further, by retaining more information existing in the input data, it enables the filtering to account for non-linear perturbation of the system due to rainfall and saturation, although at the expense of moving away from the LMMSE Wiener solutions.

The performance of the proposed filter implementation is dependent on the quality of the rainfall data, specifically its probability of detection (POD) and false alarm ratio (FAR). On one hand, when there are many false-positive identification of rainfall, the filter output will simply replicates the filter input, i.e., the output from the filtering assisted with rainfall data will have quality identical to that of the input in the limit of FAR$\to 1$. On the other hand, when there are many false-negative, the filter behaves in the way that rainfall data was not used, such that the assisted cases become the non-assisted cases in the limit of POD$\to 0$.

15

Previous evaluation studies of TMPA (3B42) aggregated daily data have shown that it is skilful in detecting the occurrence of precipitation events at daily time scales. In particular the evaluation of 3B42 (v6) over the La Plata basin in South America found that rain occurrence was best detected for low-medium thresholds of 0.1–5 mm/day with a POD> 0.7, and FAR< 0.2 (Su et al., 2008). The evaluation study of 3B42 (v7) over eastern India by Kneis et al. (2014) shows consistent results; high POD ∼ 0.8 and low FAR < 0.3 at low threshold of ∼ 5 mm. A similar result was reported by Ochoa et al. (2014) over the Pacific-Andean basin. We therefore exploit this capability of 3B42 (v7) to provide a priori knowledge of the periods Φ. The periods were distinguished using the total rainfall accumulation over 12-hour periods matching the sampling times of each satellite at each location. The accumulation was calculated by integrating the linearly interpolated 3-hourly average rainfall rates over time. Following these studies, we adopt 5 mm/12h as the the threshold for rainfall occurrence.

3.3. Method evaluation

3.3.1. Standard metrics

We first assess the merits of the de-noising schemes by their ability to improve the overall agreement between the satellite data and ground measurements. The two types of filters essentially modify the high-frequency components existing in the original timeseries, and hence the evaluation was conducted on the anomaly timeseries from 30-day moving averages following Albergel et al. (2012). Anomaly calculations were applied to untreated and post-processed data separately. Moving averages and thus the anomaly values were computed for windows containing at least 40% valid data. The traditional performance metrics typically used in evaluations (e.g., Su et al. (2013b) and references therein) are root-mean-square deviation (RMSD) and Pearson's linear correlation coefficient R between satellite (θ_S) and ground (θ_I) SM data,

$$\text{RMSD} = \sqrt{E[(\theta_I - \theta_S)^2]}, \qquad (9)$$

$$R = \frac{\text{cov}(\theta_I, \theta_S)}{\sqrt{\text{var}(\theta_I)\text{var}(\theta_S)}} \qquad (10)$$

where $E(\circ)$ specifies the expectation value in time, and $\mathrm{var}(\circ)$ and $\mathrm{cov}(\circ)$ specify the variance and covariance.

The evaluation of satellite data was conducted in their native units, i.e., volumetric soil moisture $(\mathrm{m}^3\mathrm{m}^{-3})$ for AMSR-E and percentage of saturation (%) for ASCAT. Rescaling of in situ and ERA SM was therefore needed for ASCAT evaluation; Min-max rescaling to match 0–100% range was applied to ground and ERA SM before computing their anomalies. The metrics were computed for locations with at least 100 co-located measurements, and these locations are mapped in Fig. 3.

3.3.2. Signal-to-noise ratio metric

Given that we are largely interested in reducing the noise in the satellite data, TC can provide a measure of the level of the signal relative to the level of the noise. TC uses an affine signal model and an additive orthogonal error model to relate three spatio-temporally coincident SM anomaly data from the in situ probe, satellite and ERA-Interim via,

$$\theta_q = \alpha_q + \beta_q\theta + \epsilon_q \tag{11}$$

where the subscript $q \in \{I, S, M\}$ labels the respective SM data, and θ is the unknown true, error-free SM signal common to the three SM estimates. The coefficients α_q and β_q are intercept and slope terms relating to the signal component of each data $f_q \equiv \alpha_q + \beta_q\theta$, and ϵ_q is its zero-mean noise component. The estimation equations for their variances are (Su et al., 2014a),

$$\begin{aligned}
\mathrm{var}(f_S) &= \mathrm{var}(\theta_S) - \mathrm{var}(\epsilon_S), & (12)\\
\mathrm{var}(\epsilon_S) &= \mathrm{var}(\theta_S) - \frac{\mathrm{cov}(\theta_S, \theta_I)\mathrm{cov}(\theta_S, \theta_M)}{\mathrm{cov}(\theta_I, \theta_M)}. & (13)
\end{aligned}$$

We follow the conventions of signal processing practices and Su et al. (2014b) to use signal-to-noise ratio (SNR) as the third metric. In decibel (dB), the metric SNR is computed using,

$$\mathrm{SNR} = 10\log_{10}\left[\frac{\mathrm{var}(f_S)}{\mathrm{var}(\epsilon_S)}\right]. \tag{14}$$

17

The association between RMSD and R with the variances is straightforward to understand. Substituting Eq. 11 to 9 and 10 leads to,

$$
\begin{aligned}
\text{RMSD}^2 &= [E(\theta_I) - E(\theta_S)]^2 + (\beta_I - \beta_S)^2 \text{var}(\theta) + \\
&\quad \text{var}(\epsilon_I) + \text{var}(\epsilon_S),
\end{aligned}
\tag{15}
$$

$$
R^2 = \frac{\text{var}(f_I)\text{var}(f_S)}{[\text{var}(f_I) + \text{var}(\epsilon_I)][\text{var}(f_S) + \text{var}(\epsilon_S)]}.
\tag{16}
$$

The de-noising of the satellite data aims to reduce the noise variance $\text{var}(\epsilon_S)$, which in turn reduces RMSD and increases R and SNR. Thus we also report the score changes denoted by ΔRMSD, ΔR, and ΔSNR due to the post-processing of θ_S. For TC, it requires that there are positive and substantial linear correlations between the data triplet; thus the analysis was only applied to pixels with $R(\theta_I, \theta_S), R(\theta_I, \theta_M), R(\theta_M, \theta_S) > 0.1$.

3.3.3. Comparison against precipitation data

The use of the aforementioned metrics can disguise the possibility that the satellite and in situ SM are not compatible for direct comparison at certain locations, due to marked differences in their measurement supports and high spatial heterogeneity in SM. Laterally, in situ SM are point-scale measurements c.f. mesoscale footprints ~ 50 km of the satellite microwave sensors. Vertically, the satellite sensors have shallow sensing depths up to 2 cm c.f. the placement of in situ probes at deeper depths of 0–40 cm. While these can lead to biases (as reflected by the first two terms of Eq. 9), there are also likely temporal lags between their observed SM dynamics. These differences complicate the evaluation of the performance between causal and non-causal filtering schemes as the distorted and/or over-smoothed timeseries can show better agreement with data from deeper in situ probe placements. In other words, the absence of true SM values at the representative layer of C-band sensing fundamentally limits our ability to fully assess the quality of the de-noised SM. We therefore turn to using precipitation data to provide a diagnostic examination of the filters' behaviours.

The water balance model (section 3.1.1) suggests that the positive increments

18

in SM are linearly related to precipitation p to some degree: $\Delta\theta_S \propto p$ for positive $\Delta\theta_S$. Consider then a fourth metric based on the time-lagged cross-correlation between positive $\Delta\theta_S$ and p,

$$R(p, \Delta\theta_S; \tau) = \frac{\text{cov}(p[n + \tau], \Delta\theta_S[n])}{\sqrt{\text{var}(p)\text{var}(\Delta\theta_S)}}, \tag{17}$$

where the negative (positive) time delay τ parameter corresponds to cases where p leads $\Delta\theta_S$ ($\Delta\theta_S$ leads p). Generally, SM at the shallow C-band sensing depth will show immediate response to rainfall in a 12-hour time window and thus should ideally show strong positive zero-lag correlation. Of course, there are obvious limitations to this diagnosis. The expected response will diminish with soil saturation and surface runoff, large SM variability during the 12-hour time lapse due to loss, and poor-quality rainfall data. Other wetting processes, e.g., melted snow water and irrigation, are also contributing factors, but we recall that pre-screening of the satellite data for these instances were performed. Amid these concerns, the measure of temporal association between SM and TMPA re-processed data may provide insight to the influence of different filtering schemes on the shape and timing of rainfall-induced SM increments. Specifically at each location, we identify the τ_{max} value at which $R(p, \Delta\theta_S; \tau)$ is non-zero (with p-value less than 0.01) and is maximum for all τ, and report the associated correlation value.

4. Results

Figure 2 illustrates the modifications to the original satellite SM timeseries (black dots) at the three locations due to post-processing. In general, the similarities between the satellite and in situ SM in terms of temporal responses to various rainfall events are visible, but stochastic noise is also apparent in satellite SM. The illustration of the ground measurements at 0–5 cm depth from Las Arenas in Fig. 2e and 2f also reveals the possible limitation of point-scale data, where the measured SM is not responsive to TMPA precipitation. This is in contrast to AMSR-E and ASCAT SM variability, and may be attributed to

19

either poor quality of the ground data or representativity differences between point-scale and meso-scale measurements. Hence, caution is required when interpreting RMSD and R metrics.

Gap-filling and de-noising can be distinguished as two distinctive post-processing stages, as further illustrated in Fig. 2. The gap-filled timeseries are shown by the grey curves, and the timeseries de-noised by the causal Wiener and/or bandstop filters are shown by the green and blue curves, which correspond to implementations with and without using TMPA rainfall. The differences from the original and gap-filled data are obvious; the satellite SM timeseries are considerably smoothed and the overall dynamic range is smaller, but the overall mean is preserved. The rainfall-assisted filter implementation also yields markedly different timeseries from the non-assisted counterparts, by showing more immediate and sharper response to rainfall events. The rainfall-assisted implementation can be argued to provide a more visually realistic SM timeseries.

The subsequent sections detail our quantitative evaluation of gap-filling and de-noising, separately. The influence of gap-filling on the agreement between the satellite and in situ data is shown in Fig. 4, and the effect of de-noising for AMSR-E and ASCAT in Figs. 5 and 6 respectively. The spatial statistics of the scores for various de-noising implementations are summarized in Tab. 1. To take into consideration different scores at different evaluation sites, we present the spatial summary statistics, namely the median and interquartile range (IQR) statistics of the scores (or differences in score), using a bracket notation *median[IQR]*, e.g., 0.05[1] refers to median of 0.05 and IQR of 0.01. Finally the lag-correlation analyses are presented in Fig. 7.

4.1. Evaluation of gap-filled satellite data

There is a high incidence of missing values in half-daily, AMSR-E and AS-CAT SM timeseries. However, for the pixels evaluated in Figure 4, the continuous data gaps mainly have lengths $\leq$ 2-days for $>$ 80% of the gaps. Consequently, the applications of the gap-filling algorithm results in $(L_{\mathrm{interp}} + L_{\mathrm{orig}}/L_{\mathrm{orig}}) = 1 - 2.5$ fold increase in the effective satellite SM sample size

$L = L_{\text{interp}} + L_{\text{orig}}$. ASCAT needs more interpolation than AMSR-E because of its longer revisit time.

As a baseline, the original AMSR-E SM has RMSD=0.063[23] m^3m^{-3}, R=0.29[20] and SNR=-3.9[60] dB, while ASCAT has 13.6[29]%, 0.46[20] and -0.49[40] dB, respectively. After gap-filling, the overall changes in scores are small. The noticeable difference is related to ASCAT, showing ΔSNR of -1.1[15] dB, compared to 0.1[6] dB for AMSR-E.

In repeated analyses (not shown), we distinguish between the existing data from the interpolated data, and find more striking differences in their quality. The interpolated data show lower RMSD, by -0.03[2] m^3m^{-3} for AMSR-E and -2.4[21]% for ASCAT, when compared to the existing data. The results are mixed for other metrics. The interpolated AMSR-E data shows higher R by 0.10[10] and SNR by 2.5[28] dB, whereas interpolated ASCAT data shows marginally lower R and SNR by -0.03[11] and -1.7[26] dB respectively.

4.2. Evaluation of de-noised AMSR-E SM

Figure 5 shows the quality of AMSR-E SM data following the application of bandstop (labeled with 'B') and Wiener causal ('C') or non-causal ('NC') filtering, but without using the rainfall data. The reference scores are taken from the evaluation of the gap-filled data, which has RMSD=0.056[19] m^3m^{-3}, R=0.30[20] and SNR=-3.7[60] dB. All the sites show improvements in RMSD, and only few sites (up to 7) show degradation in R and SNR. The overall improvements are apparent: ΔRMSD=-0.02 m^3m^{-3}, ΔR=0.13-0.14 and ΔSNR = 4.5-5 dB. The change in SNR corresponds to 2.8-3.2-fold increase in the signal variance relative to the noise variance in the de-noised data. The locations with larger initial RMSD and lower initial SNR show greater improvements in these metrics.

Table 1 summarises the evaluation of de-noised AMSR-E SM produced by different combinations of the bandstop filter, the Wiener filters, with (labeled with 'R') and without the use of TMPA rainfall data. The first set of columns show the results from evaluating all (interpolated and existing) satellite SM val-

21

ues. On the whole, the improvements are largest amongst the implementations involving the Wiener filters without TMPA data, and the bandstop filtering yields marginal reduction in RMSD and modest increase in R and SNR. The non-causal filtering produced slightly better scores than the causal filtering. The use of TMPA data typically diminishes the overall agreement between de-noised satellite and in situ data.

Separate evaluations of the interpolated and existing data are reported in the subsequent columns of Table 1. It is found that the improvements previously observed in the all-data evaluation are largely due to improvements in the existing data, and the merits of using the bandstop filter become more apparent. For the existing data, the bandstop filtering leads to $\Delta R = 0.06[4]$ and ΔSNR=2.0[12] dB, and combined with the Wiener filtering, ΔRMSD$\sim$ $-0.03[2]$ m^{3}m^{-3}, $\Delta R \sim 0.16[8]$ and ΔSNR$\sim 5.5[24]$ dB. The interpolated data are also enhanced by de-noising, but with more modest increases in R and SNR. This is partly because the quality of the interpolated data is better than the existing data before de-noising (see section 4.1). Even so, de-noising can be seen to be complementary to interpolation, to further improve the accuracy of the estimated SM during non-retrieval times.

4.3. Evaluation of de-noised ASCAT SM

Figure 6 shows the evaluation of the ASCAT de-noised by the Wiener filters. The median and IQR statistics of RMSD, R and SNR of the gap-filled ASCAT are 12.3[25]%, 0.43[18], and -1.5[38] dB, respectively. All locations show clear improvements in RMSD and SNR, but for the non-causal Wiener implementation, up to 19 sites (out of 385) show negative ΔR and 6 sites show negative ΔSNR. Comparing against AMSR-E, the magnitude of the improvements is also generally smaller: ΔRMSD$\sim -1.6\%$, ΔR=0.04–0.09 and ΔSNR=1.4–2.7 dB, corresponding to 1.4-1.9-fold increase in signal variance relative to noise variance. The smaller gain is expected because the gap-filled ASCAT SM has better agreement with in situ data than the AMSR-E SM, prior to de-noising. The other difference from the AMSR-E data is that the use of causal filtering on

22

the ASCAT data outperforms the use of non-causal filtering in terms of R and SNR.

Other filter implementations are summarised in Table 1. The greatest improvements are found amongst the existing data with the causal filtering, with $\Delta R = 0.09[5]$ and ΔSNR=3[2] dB. For the interpolated ASCAT data, the improvements are greater than the interpolated AMSR-E data. Furthermore, the use of rainfall data appears to benefit the non-causal filtering approach in terms of R and SNR.

4.4. Evaluation against precipitation data

Figure 7 shows the lag correlation analysis between TMPA precipitation p and positive SM increments $\Delta\theta_*$ observed in in situ data (7a,g) and satellite data (7b-f for AMSR-E and 7h-l for ASCAT). For each SM data, the lag $\tau_{\max}$ value that maximizes its cross correlation with p is identified at each site, and the sites with same $\tau_{\max}$ are binned. The boxplots show the range of $R(p, \Delta\theta_*; \tau_{\max})$ values within each bin. Ideally, the shallow SM, as was observed by C-band sensors, should show short-time scale and coincident response to precipitation, and this should manifest as strong lag-zero cross correlation if the linear dynamics in SM is dominant and precipitation data is representative.

At most sites, the ground data have their highest correlation at zero lag, and the median of the $R(p, \Delta\theta_I; \tau = 0)$ is 0.47. The relatively strong correlations suggest that there are some merits of using the TMPA data to evaluate satellite SM. In reference to the example timeseries in Fig. 2, the in situ measurements show stronger lag-zero $R(p, \Delta\theta_I)$ of 0.45 at Cooma airfield and 0.55 at Little River, compared to 0.23 at Las Arenas where differences between θ_I and p are apparent. Over 50 sites appear to show lagged responses to TMPA, which may be attributed to the differences in (lateral and vertical) measurement supports (e.g., Fig. 2e,f), poor data quality and/or nonlinear SM processes. We also note that when $R(p, \Delta\theta_I; \tau)$ becomes too weak, the lag $\tau_{\max}$ is generally ill-defined, such that in some cases has values outside of the plot range.

For the pre-denoised satellite SM in Fig. 7b and h, most pixels similarly

23

show maximum correlations $R(p, \Delta\theta_S; \tau)$ at zero lag, but the median of correlation statistics is relatively lower at 0.2 for AMSR-E and 0.27 for ASCAT. In addition to the above reasons, the presence of noise can suppress the correlation with rainfall, since it will manifest as both false positive and false negative SM increments.

The rest of the panels in Fig. 7 illustrates the influence of de-noising on the cross-correlation. In particular, we find that the non-assisted causal Wiener filtering, which shifts the filter output forward in time relative to its input, increases the number of sites with negative $\tau_{\max}$ for AMSR-E (7c). In other words, the de-noised AMSR-E shows increased delayed response to precipitation. The problem of over-smoothing by the non-causal Wiener filtering also becomes apparent from the increased number of sites with positive $\tau_{\max}$ (7d and 7j); the de-noised SM at these sites therefore show non-causal response to precipitation. Such degradation of the satellite SM is not apparent in the traditional metrics.

The influence of using rainfall in the filtering is shown in Fig. 7e-f (AMSR-E) and k-l (ASCAT). It leads to stronger zero-lag correlations at almost all the satellite pixels, where median $R(p, \Delta\theta_S; \tau = 0)$ statistics are 0.47–0.55, and all the sites show maximum correlation between $\Delta\theta_S$ and p at zero-lag. These results are consistent with the qualitative differences between non-assisted and assisted filtering observed in Fig. 2.

5. Discussion and conclusion

The functionalities of de-noising Fourier filters under investigation are intuitive to understand. The Wiener filters are low-pass filters that attenuate high-frequency spectral components in the data where noise is most prominent. This gives rise to smoothing of the input timeseries. The bandstop filters are designed to remove extraneous spectral peaks, which represent a form of systematic errors in satellite SM. The reference spectrum of an error-free SM needed to identify these high-frequency noise and extraneous peaks is provided by the Fourier transform of the governing water-balance equation. The key advantages

24

of these filters over other low-pass (e.g., moving-average or median) filters are that they were not designed in an ad-hoc fashion but based on a physical model, and practically, their calibration does not require ancillary data.

Based on anomaly-based evaluation metrics (RMSD, R and SNR), the post-processed data were evaluated against ISMN at over 270 locations for AMSR-E and over 380 locations for ASCAT. In particular, before post-processing, the median statistics for RMSD, R and SNR are 0.06 m^3m^{-3}, 0.29 and -3.9 dB for AMSR-E, and 14% (in units of degree of saturation), 0.46, and -0.49 dB for AS-CAT. While there is significant variability in data quality across different sites, the relatively low scores support our rationale for post-processing to improve their qualities.

Given an intermittent data stream, we used the DCT-based gap-filling algorithm of Garcia (2010) to estimate missing SM values in gaps of $\leq$ 2-days. We found in section 4.1 that interpolation over few-day gaps appears to provide reasonable SM estimates with some agreement with in situ data. Notably, the accuracy of the interpolated data is commensurate with or even slightly better than the existing data, especially for the AMSR-E data that contains shorter gaps than the ASCAT data. For instance, interpolated AMSR-E SM values have lower RMSD by (median statistics) 0.03 m^3m^{-3}, higher R by 0.10 and SNR by 2.5 dB, relative to existing SM data. Given that the interpolation algorithm uses the spectral characteristics of the entire timeseries, the resultant SM estimates can retain the autocorrelation nature of SM but are also smoothed. This may be responsible for better agreement between interpolated satellite data and in situ data. However, it is expected that their accuracy of the interpolated data will diminish with longer gaps and during periods of high SM variability. Future studies may trial different interpolation algorithms and investigate the dependency of their performance on the gap length and SM autocorrelation length.

With respect to de-noising, we found in section 4.2 and 4.3 that the systematic improvements of the satellite data came from the bandstop and Wiener filtering, and greater enhancement was found to be amongst the existing data

(as opposed to interpolated data). For instance, the de-noised AMSR-E SM reported improved scores of (median statistics) ΔRMSD=-0.02 m^{3}m^{-3}, $\Delta R = 0.13 - 0.14$ and ΔSNR= $4.5 - 5$ dB, whereas de-noised ASCAT reported -1.6%, $0.04 - 0.09$ and 1.4–2.7 dB, respectively. In other words, the magnitudes of over-all improvement are greater amongst AMSR-E data than the ASCAT because the latter shows better agreement with in situ data prior to de-noising, although their associated evaluation sites and periods are notably different. More generally, the results highlight the fact that high-frequency noise diminishes the quality of the satellite data, and by removing them through filtering, their quality can be enhanced. The implementations without using rainfall data generally offer better agreement based on the traditional evaluation metrics (RMSD, R and SNR). This finding, however, must be viewed in the context of the problematic over-smoothing and distortion of the SM timeseries by the non-assisted filtering. Better agreement in terms of these three metrics can disguise such adverse filtering effects.

By examining the lag-correlations between positive SM increments and precipitation in section 4.4, the differences between various filter implementations became discernible. We found evidence of these adverse effects amongst non-assisted filter implementations. More importantly, we demonstrated a possible resolution from using the precipitation data to alleviate the problem of over-smoothing due to the filters' LTI characteristics and the LMMSE formalism, and reduce distortion caused by the causal filters' phase characteristics. In particular, the SM increments in the (assisted) de-noised products show desirable enhanced lag-zero cross-correlation, which is indicative of retained short-time scale SM variability; this is also visible in the timeseries plots (Fig. 2). By using only the categorical rain/no-rain information in the TMPA, the method is expected to be less susceptible to its associated biases and errors. The proof-of-concept evaluation using satellite-retrieved rainfall data is further encouraged by the global availability of such data that is expected to continue with the Global Precipitation Measurement mission (Smith et al., 2007), in addition to relatively widespread rain-gauge networks globally.

26

The greatest improvements of the satellite data came from the Wiener filtering, but the relative merits between causal and non-causal filtering are not consistent between the two SM products. For AMSR-E, while the phase-shift characteristics of the causal filter could conceivably cause the shallow AMSR-E SM to reflect deeper SM observations better, this is not apparent in our causal c.f. non-causal comparison in terms of the traditional metrics. Furthermore, the lag-correlation analysis suggests that both causal and non-causal filtering are problematic with AMSR-E SM. For ASCAT, the causally-filtered SM shows better overall agreement with the in situ data and stronger lag-zero correlation with TMPA data. A likely reason is the algorithmic differences between the SM products in terms of the retrieval model and the model inversion strategy, since the ASCAT has similar vertical sampling depth sensitivity to the AMSR-E. Further investigation is still needed to understand the influence of retrieval algorithms and different measurement supports on the perceived SM variability. Based on our lag-correlation results, we recommend assisted non-causal filtering, unless restricted by real-time operational requirement.

In relation to the broader literature on model-data assimilation, the Kalman filtering and smoothing generalise the causal and non-causal Wiener filters to appreciate time-varying characteristics in underlying model, model and observational errors. They also allow better integration of SM data and many other observational data e.g., via a land-surface model. In this work, using rainfall data to dynamically modify the Fourier filtering process represents a partial solution and a bold (perhaps, ad-hoc) step beyond the standard approach, in the direction towards the more sophisticated Kalman-based approaches. However the success of the data assimilation depends on a model that appropriately accounts for the nonlinear SM dynamics, knowledge of soil properties at multiple depths, proper characterisation of model and observational errors, and accurate observational operators relate observed variables to their modelled counterparts. While significant advances have been made in this direction (e.g. Dunne & Entekhabi, 2005; Draper et al., 2012), our approach is practically simple to implement, generating SM data sets that are very close to observations

27

and can be an important complement to modelled data and re-analysis. Looking ahead, the adopted Fourier filter designs may be improved with better under-

₇₄₀ standing of the spectral characteristics of the satellite SM errors. In turn, such understanding can advise optimal land data assimilation of satellite SM.

In conclusion, this work found compelling evidence that the Fourier (Wiener and bandstop) filters have skill in improving existing satellite active and passive microwave SM products. Without the minimal need for ancillary data, the

₇₄₅ schemes can potentially be applied to a broad range of historical satellite SM records (from 1978) and in causal forms, are relevant to future observations and use in operational environments. The filters are support-independent and thus are applicable for other sources of SM estimates from in situ sensors and models.

References

Albergel,C., De Rosnay, P., Gruhier, C., Muñoz-Sabater, J., Hasenauer, S., Isaksen, L., Kerr, Y., & Wagner, W. (2012). Evaluation of remotely sensed and modelled soil moisture products using global ground-based in situ observations. Remote Sensing of Environment, 118, 215–226.

Albergel, C., Rüdiger, C., Pellarin, T., Calvet, J.-C., Fritz, N., Froissard, F., et al. (2008). From near-surface to root-zone soil moisture using an exponential filter: an assessment of the method based on in-situ observations and model simulations. Hydrology and Earth System Sciences, 12(6), 1323–1337.

Arino, O., Gross, D., Ranera, F., Bourg, L., Leroy, M., Bicheron, P., et al. (2007). GlobCover: ESA service for global land cover from MERIS. IEEE International Geoscience and Remote Sensing Symposium (IGARSS 2007), 2412–2415.

Brocca, L., Moramarco, T., Melone, F., Wagner, W., Hasenauer, S., & Hahn, S. (2012). Assimilation of surface- and root-zone ASCAT soil moisture products into rainfall-runoff modeling. IEEE Transactions on Geoscience and Remote Sensing, 50(7), 2542–2555.

Crow, W. T., & Ryu, D. (2009). A new data assimilation approach for improving runoff prediction using remotely-sensed soil moisture retrievals. Hydrology and Earth System Sciences, 13(1), 1–16.

Dee, D. P., Uppala, S. M., Simmons, A. J., Berrisford, P., Poli, P., Kobayashi, S., et al. (2011). The ERA-Interim reanalysis: configuration and performance of the data assimilation system. Quarterly Journal of the Royal Meteorological Society, 137(656), 553–597.

Dorigo, W. A., Scipal, K., Parinussa, R. M., Liu, Y. Y., Wagner, W., de Jeu, R. A.M., et al. (2010). Error characterisation of global active and passive microwave soil moisture datasets. Hydrology and Earth System Sciences, 14, 2605–2616.

Dorigo, W. A., Wagner,W., Hohensinn, R., Hahn, S., Paulik, C., Xaver, A., et al. (2011). The International Soil Moisture Network: A data hosting facility for global in situ soil moisture measurements. Hydrology and Earth System Sciences, 15, 1675–1698.

Dorigo, W.A., Xaver, A., Vreugdenhil, M., Gruber, A., Hegyiová, A., Sanchis-Dufau, A.D., et al. (2013). Global automated quality control of in situ soil moisture data from the International Soil Moisture Network. Vadose Zone Journal, 12(3).

Draper, C. S., Reichle, R. R., De Lannoy, G. J. M., & Liu, Q. (2012). Assimilation of passive and active microwave soil moisture retrievals. Geophysical Research Letters, 39(4), L04401.

Draper, C. S., Reichle, R. R., de Jeu, R. A., Naeimi, V., Parinussa, R. M., & Wagner, W. (2013). Estimating root mean square errors in remotely sensed soil moisture over continental scale domains. Remote Sensing of Environment, 137, 288–298.

Du, J. (2012). A method to improve satellite soil moisture retrievals based on Fourier analysis. Geophysical Research Letters, 39(15), L15404.

Drusch, M., Wood, E. F., & Gao, H. (2005). Observation operators for the direct assimilation of TRMM microwave imager retrieved soil moisture, Geophysical Research Letters, 32(15), L15403.

Dunne, S., & Entekhabi, D. (2005). An ensemble-based reanalysis approach to land data assimilation, Water Resources Research, 41(2), W02013.

Entekhabi, D., Njoku, E.G., O'Neill, P.E., Kellogg, K.H., Crow, W.T., Edelstein, W.N., et al. (2010). The Soil Moisture Active Passive (SMAP) mission. Proceedings of the IEEE, 98(5), 704–716.

Garcia, D. (2010). Robust smoothing of gridded data in one and higher dimensions with missing values. Computational Statistics and Data Analysis, 54, 1167–1178.

Gruber, A., Dorigo, W.A., Zwieback, S., Xaver, A., & Wagner, W. (2013). Characterizing coarse-scale representativeness of in situ soil moisture measurements from the International Soil Moisture Network. Vadose Zone Journal, 12(2).

Huffman, G. J., Bolvin, D. T., Nelkin, E. J., Wolff, D. B., Adler, R. F., Gu, G., et al. (2007). The TRMM Multisatellite Precipitation Analysis (TMPA): Quasiglobal, multiyear, combined-sensor precipitation estimates at fine scales. Journal of Hydrometeorology, 8, 38–55.

Imaoka, K., Kachi, M., Fujii, H., Murakami, H., Hori, M., Ono, A., et al. (2010). Global Change Observation Mission (GCOM) for monitoring carbon, water cycles, and climate change. Proceedings of the IEEE, 98(5), 717–734.

Jackson, T. J., Cosh, M. H., Bindlish, R., Starks, P. J., Bosch, D. D., Seyfried,M., et al. (2010). Validation of Advanced Microwave Scanning Radiometer soil moisture products. IEEE Transactions on Geoscience and Remote Sensing, 48(12), 4256-4272.

Katul, G. G., Porporato, A., Daly, E., Oishi, A.C., Kim, H. -S., Stoy, P. C., et al. (2007). On the spectrum of soil moisture from hourly to interannual scales. Water Resource Research, 43, W05428.

Kerr, Y.H., Waldteufel, P., Wigneron, J.-P., Martinuzzi, J., Font, J., & Berger, M. (2001). Soil moisture retrieval from space: the Soil Moisture and Ocean Salinity (SMOS) mission. IEEE Transactions on Geoscience and Remote Sensing, 39(8), 1729–1735.

Kneis, D., Chatterjee, C., & Singh, R. (2014). Evaluation of TRMM rainfall estimates over a large Indian river basin (Mahanadi). Hydrology and Earth System Sciences, 18(7), 2493–2502.

Kumar, S. V., Reichle, R. H., Harrison, K. W., Peters-Lidard, C. D., Yatheendradas, S., & Santanello, J. A. (2012). A comparison of methods for a priori

bias correction in soil moisture data assimilation, Water Resource Research, 48, W03515.

Lehner, B., & Döll, P. (2004). Development and validation of a global database of lakes, reservoirs and wetlands. Journal of Hydrology, 296(1–4), 1–22.

Ochoa, A., Pineda, L., Crespo, P., & Willems, P. (2014). Evaluation of TRMM 3B42 precipitation estimates and WRF retrospective precipitation simulation over the PacificAndean region of Ecuador and Peru. Hydrology and Earth System Sciences, 18(8), 3179–3193.

Owe, M., de Jeu, R., & Holmes, T. (2008). Multisensor historical climatology of satellite-derived global land surface moisture, Journal of Geophysical Research, 113, F01002.

Mladenova, I.E., Jackson, T.J., Njoku, E., Bindlish, R., Chan, S., Cosh, M.H., et al. (2014). Remote monitoring of soil moisture using passive microwave-based techniques Theoretical basis and overview of selected algorithms for AMSR-E. Remote Sensing of Environment, 144, 197–213.

Naeimi, V., Scipal, K., Bartalis, Z., Hasenauer, S., & Wagner, W. (2009). An improved soil moisture retrieval algorithm for ERS and METOP scatterometer observations. IEEE Transactions on Geoscience and Remote Sensing, 47(7), 1999–2013.

Njoku, E.G., Jackson, T.J., Lakshmi, V., Chan, T.K., & Nghiem, S.V. (2003). Soil moisture retrieval from AMSR-E. IEEE Transactions on Geoscience and Remote Sensing, 41(2), 215–229.

Salvucci, G. D. (2001). Estimating the moisture dependence of root zone water loss using conditionally averaged precipitation. Water Resources Research, 37(5), 1357–1365.

Sang, Y.-F., Wang, D., Wu, J.-C., Zhu, Q.-P., & Wang, L. (2009). Entropy-based wavelet de-noising method for time series analysis. Entropy, 11(4), 1123–1147.

Scipal, K., Drusch, M., & Wagner, W. (2008a). Assimilation of a ERS scatterometer derived soil moisture index in the ECMWF numerical weather prediction system, Advances in Water Resoures, 31(8), 1101–1112.

Scipal, K., Holmes, T., de Jeu, R., Naeimi, V., & Wagner, W. (2008b). A possible solution for the problem of estimating the error structure of global soil moisture data sets. Geophysical Research Letters, 35(24), L24403.

Smith, E.A., Asrar, G., Furuhama, Y., Ginati, A., Mugnai, A., Nakamura, K., et al. (2007). The International Global Precipitation Measurement (GPM) program and mission: An overview. *Measuring Precipitation from Space: URAINSAT and the Future*, V. Levizzani and F. J. Turk, Eds., The Netherlands: Springer, 611–653.

Su, F., Hong, Y., & Lettenmaier, D. P. (2008). Evaluation of TRMM Multisatellite Precipitation Analysis (TMPA) and its utility in hydrologic prediction in the La Plata Basin. Journal of Hydrometeorology, 9(4), 622–640.

Su, C.-H., Ryu, D., Western, A. W., & Wagner, W. (2013a). De-noising of passive and active microwave satellite soil moisture time series. Geophysical Research Letters, 40(14), 3624–3630.

Su, C.-H., Ryu, D., Young, R. I., Western, A. W., & Wagner, W. (2013b). Inter-comparison of microwave satellite soil moisture retrievals over the Murrumbidgee Basin, southeast Australia. Remote Sensing of Environment, 134, 1–11.

Su, C.-H., Ryu, D., Crow, W. T., & Western, A. W. (2014a). Beyond triple collocation: Applications to soil moisture monitoring. Journal of Geophysical Research: Atmospheres, 119(11), 6419–6439.

Su, C.-H., Ryu, D., Crow, W. T., & Western, A. W. (2014b). Stand-alone error characterisation of microwave satellite soil moisture using a Fourier method. Remote Sensing of Environment, 154, 115–126.

Su, C.-H., & Ryu, D. (2015). Multi-scale analysis of bias correction of soil moisture. Hydrology and Earth System Sciences, 19(1), 17–31.

Wagner, W., Lemoine, G., & Rott, H. (1999). A method for estimating soil moisture from ERS scatterometer and soil data. Remote Sensing of Environment, 70(2), 191–207.

Wagner, W., Hahn, S., Kidd, R., Melzer, T., Bartalis, Z., Hasenauer, S., et al. (2013). The ASCAT soil moisture product: A review of its specifications, validation results, and emerging applications. Meteorologische Zeitschrift, 22(1), 5–33.

Wagner, W., Brocca, L., Naeimi, V., Reichle, R., Draper, C., De Jeu, R., et al. (2014). Clarifications on the "Comparison Between SMOS, VUA, ASCAT, and ECMWF Soil Moisture Products Over Four Watersheds in U.S". IEEE Transactions on Geoscience and Remote Sensing, 52(3), 1901–1906.

Wang, G., Garcia, D., Liu, Y., De Jeu, R., & Dolman, A. J. (2012). A three-dimensional gap filling method for large geophysical datasets: Application to global satellite soil moisture observations. Environmental Modelling & Software, 30, 139–142.

Wiener, N. (1964). Extrapolation, Interpolation, and Smoothing of Stationary Time Series: With Engineering Applications. USA: The M.I.T. Press.

Yilmaz, M. T., Crow, W. T., Anderson, M. C., & Hain, C. (2012). An objective methodology for merging satellite- and model-based soil moisture products. Water Resources Research, 48(11), W11502.

Yilmaz, M. T., & Crow, W. T. (2013). The optimality of potential rescaling approaches in land data assimilation. Journal of Hydrometeorology, 14(2), 650–660.

Massari, C., Brocca, L., Ciabatta, L., Moramarco, T., Su, C.-H., Ryu, D., & Wagner, W. (2014). A Wiener-wavelet-based filter for de-noising satellite soil

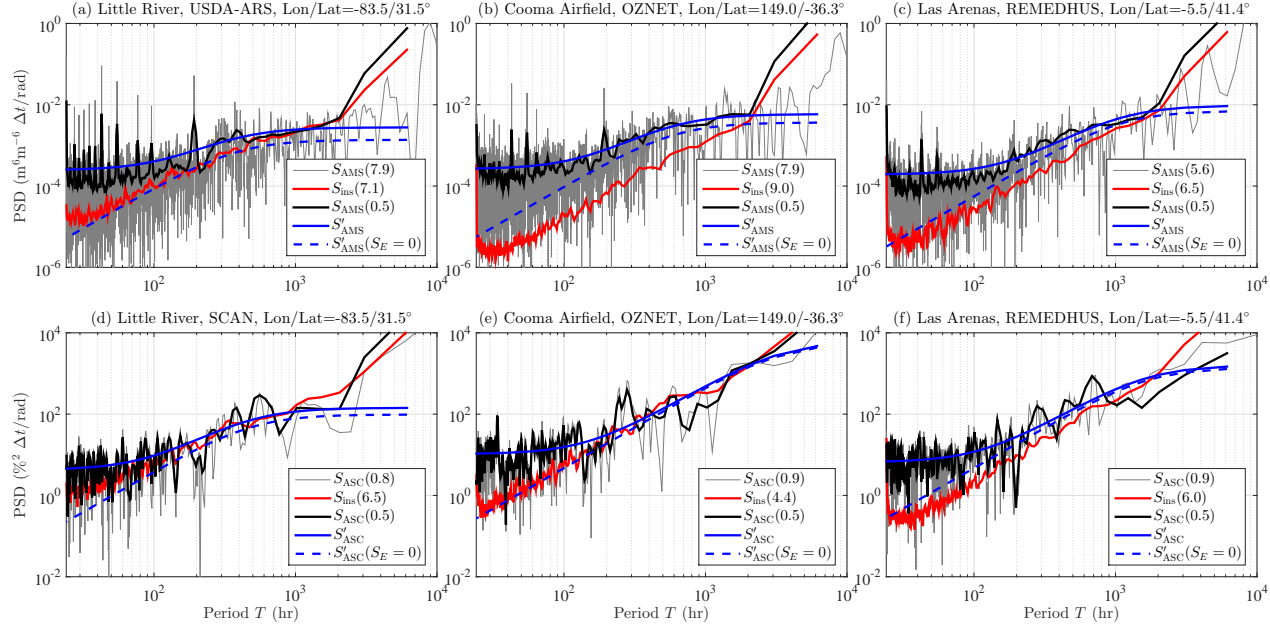moisture retrievals. Geophysical Research Abstracts, EGU General Assembly 2014, 16, EGU2014–3940.

Figure 1: Spectral analysis of satellite (black and grey curves) and in situ (red) SM, showing the PSD of the AMSR-E (S_{AMS}) (a-c) and ASCAT (S_{ASC}) SM (d-f) at three monitoring locations. They are compared with the PSD of the co-located in situ SM (S_{ins}). Brackets in legend indicate the size of the Hamming window in units of years used for PSD estimation. S_{ins} differs because different data are used to match different satellite periods. Blue curves are the model S' (Eq. 3) fitted to the satellite PSD for instances with and without noise term S_E.
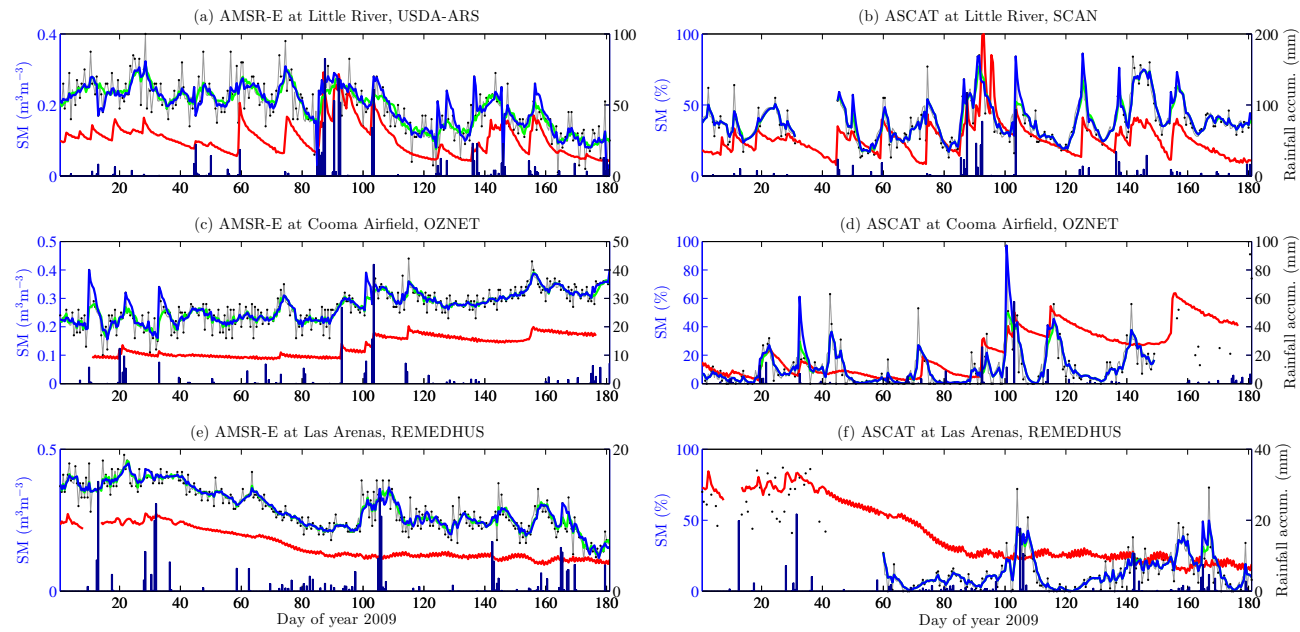
Figure 2: Untreated and treated AMSR-E and ASCAT SM. Black dots are original SM data points, grey curves are gap-filled SM, and green (blue) curves are de-noised SM with causal filter (with TMPA rainfall). Red dots are the in situ SM data. The superimposed bar plots are 12-hourly TMPA rainfall accumulation.
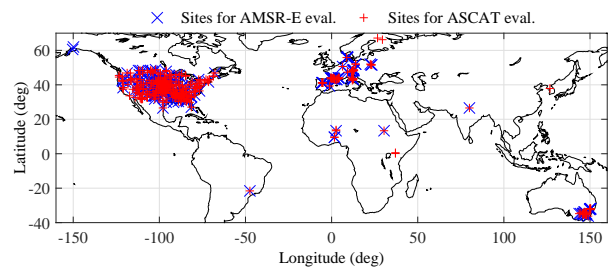
Figure 3: Locations of the selected evaluation sites for original and post-processed AMSR-E and ASCAT SM.
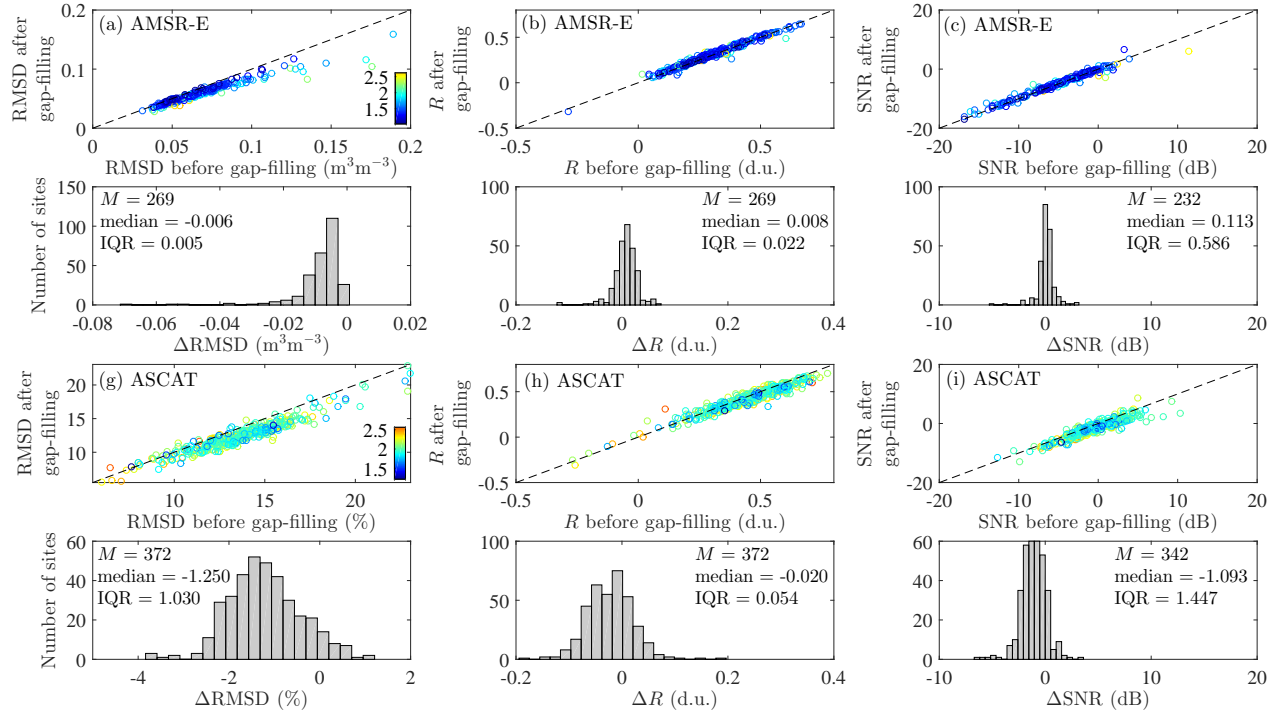
Figure 4: Evaluation of gap-filled satellite SM anomalies against in situ SM anomalies, in terms of RMSD, correlation R and SNR. For the scatterplots, x-axes denote the scores of the untreated satellite SM, and y-axes the score after gap-filling. Each symbol corresponds to one evaluation site amongst M total number of sites. The color coding indicates the multiplicative increase in the length of satellite anomaly data for evaluation due to gap filling. The barplots show the changes in scores across all sites, and indicate spatial median and interquartile range (IQR) statistics of the score change.
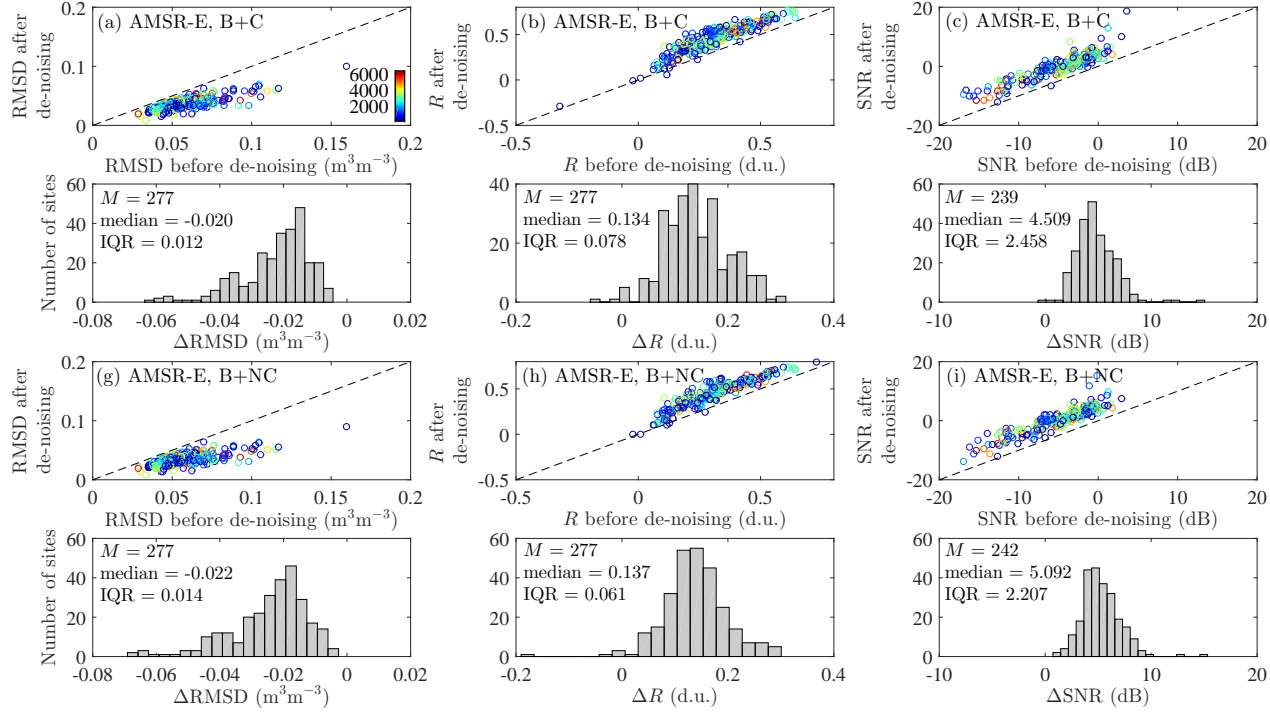
Figure 5: Evaluation of de-noised, gap-filled AMSR-E SM anomalies against in situ SM anomalies. Two sets of filters were applied, namely bandstop ('B') and Wiener causal ('C') or non-causal ('NC') filters. TMPA rainfall data were not used. The color coding indicates the size of sample evaluated at each site. Computation of M, median, and IQR follows Fig. 4.
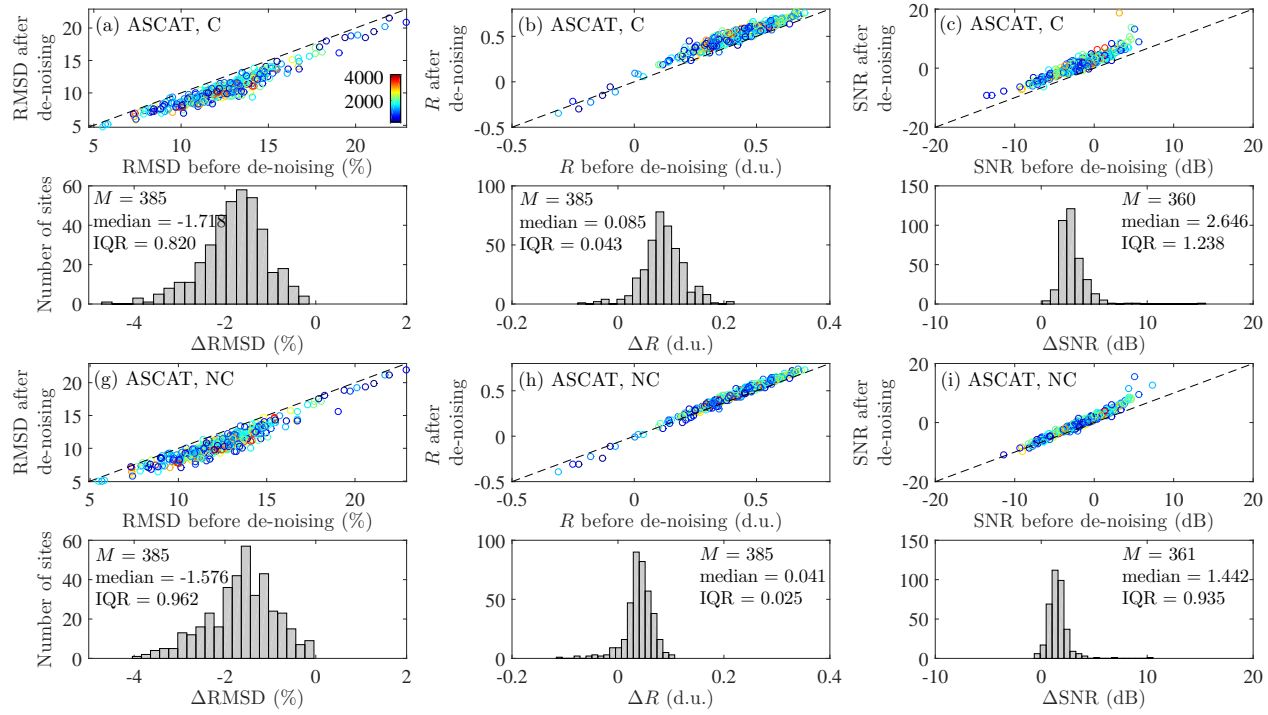
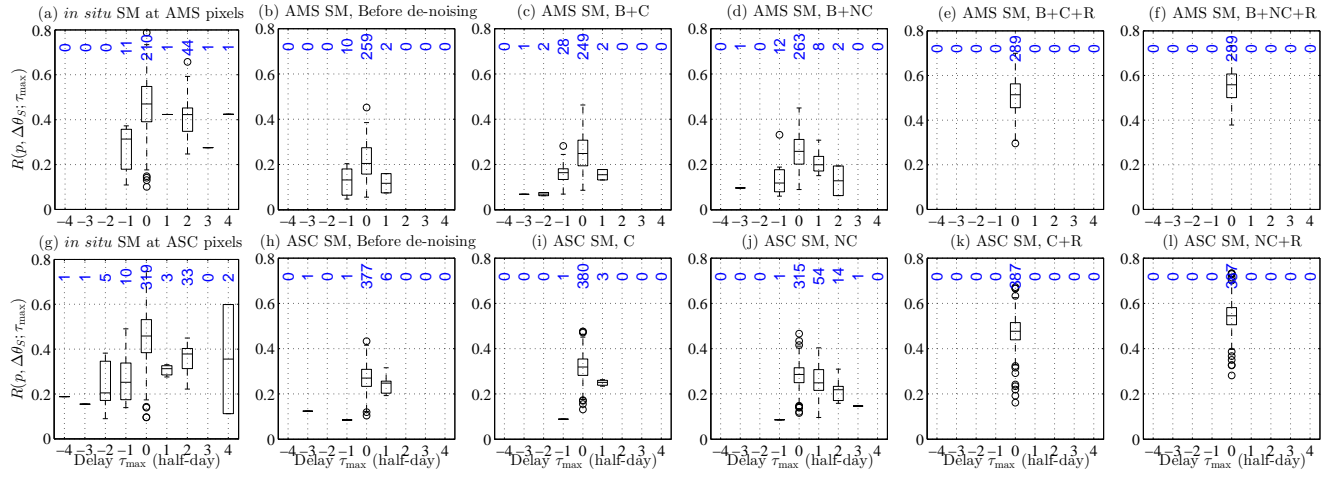Figure 6: Same as Fig. 5, but for ASCAT and bandstop filter was not used.

Figure 7: Statistics of maximum lag-correlation between TMPA precipitation and positive SM increments in each SM data set. (a,g) shows the analysis for in situ SM data; (b,h) for satellite SM before de-noising; (rest) for satellite SM after de-noising. The blue integers are number of sites for each $\tau_{\max}$ bin.

Table 1: Summary of changes to the scores after applying de-noising to gap-filled satellite data. The filter notations follow Fig. 5, and label 'R' corresponds to cases where TMPA rainfall data was used. The bracket notation refers to *median[IQR]* statistics. ΔRMSD is in units of m^3m^{-3} (%) for AMSR-E (ASCAT), and ΔSNR is in units of dB.

		All data			Interpolated data			Existing data		
Prod.	Filt.	ΔRMSD	ΔR	ΔSNR	ΔRMSD	ΔR	ΔSNR	ΔRMSD	ΔR	ΔSNR
AMS	B	-0.008[7]	0.046[29]	1.6[11]	0.003[3]	-0.026[40]	-1.1[12]	-0.012[9]	0.057[36]	2.0[12]
	B+R	-0.005[5]	0.033[27]	1.2[8]	0.002[3]	-0.012[37]	-0.5[13]	-0.007[6]	0.035[28]	1.3[9]
	B+C	-0.020[12]	0.134[78]	4.5[25]	-0.001[2]	0.032[62]	0.6[15]	-0.026[17]	0.158[86]	5.4[24]
	B+C+R	-0.013[10]	0.102[75]	3.6[20]	0.001[5]	0.034[66]	0.9[17]	-0.018[13]	0.117[76]	4.0[20]
	B+NC	-0.022[14]	0.137[61]	5.1[22]	-0.002[2]	0.029[21]	1.1[6]	-0.029[17]	0.162[73]	6.0[24]
	B+NC+R	-0.018[11]	0.117[64]	4.2[19]	-0.002[2]	0.045[40]	1.7[11]	-0.024[15]	0.127[70]	4.7[21]
ASC	C	-1.72[82]	0.085[43]	2.7[12]	-0.67[42]	0.071[41]	2.2[11]	-2.92[141]	0.087[46]	3.1[18]
	C+R	-1.23[55]	0.073[36]	2.3[9]	-0.50[45]	0.068[38]	2.1[9]	-1.97[93]	0.069[40]	2.4[12]
	NC	-1.58[96]	0.041[25]	1.4[9]	-0.38[26]	0.024[14]	1.0[4]	-2.96[159]	0.052[41]	1.8[15]
	NC+R	-1.44[72]	0.052[24]	1.7[9]	-0.52[28]	0.042[22]	1.5[6]	-2.52[128]	0.052[30]	1.8[12]